



LAWRENCE  
LIVERMORE  
NATIONAL  
LABORATORY

# Sub-discretized surface model with application to contact mechanics in multi-body simulation

S. Johnson, J. Williams

February 29, 2008

Powder Technology

## **Disclaimer**

---

This document was prepared as an account of work sponsored by an agency of the United States government. Neither the United States government nor Lawrence Livermore National Security, LLC, nor any of their employees makes any warranty, expressed or implied, or assumes any legal liability or responsibility for the accuracy, completeness, or usefulness of any information, apparatus, product, or process disclosed, or represents that its use would not infringe privately owned rights. Reference herein to any specific commercial product, process, or service by trade name, trademark, manufacturer, or otherwise does not necessarily constitute or imply its endorsement, recommendation, or favoring by the United States government or Lawrence Livermore National Security, LLC. The views and opinions of authors expressed herein do not necessarily state or reflect those of the United States government or Lawrence Livermore National Security, LLC, and shall not be used for advertising or product endorsement purposes.

**Sub-discretized surface model with application to contact mechanics in multi-body simulation****Scott M. Johnson***Lawrence Livermore National Laboratory, Livermore, California, USA 94551***John R. Williams***Massachusetts Institute of Technology, Cambridge, Massachusetts, USA 02139***Abstract:**

The mechanics of contact between rough and imperfectly spherical adhesive powder grains are often complicated by a variety of factors, including several which vary over sub-grain length scales. These include several traction factors that vary spatially over the surface of the individual grains, including high energy electron and acceptor sites (electrostatic), hydrophobic and hydrophilic sites (electrostatic and capillary), surface energy (general adhesion), geometry (van der Waals and mechanical), and elasto-plastic deformation (mechanical). For mechanical deformation and reaction, coupled motions, such as twisting with bending and sliding, as well as surface roughness add an asymmetry to the contact force which invalidates assumptions for popular models of contact, such as the Hertzian and its derivatives [1-3], for the non-adhesive case, and the JKR [4] and DMT [5] models for adhesive contacts. Though several contact laws have been offered to ameliorate these drawbacks, they are often constrained to particular loading paths (most often normal loading) and are relatively complicated for computational implementation. This paper offers a simple and general computational method for augmenting contact law predictions in multi-body simulations through characterization of the contact surfaces using a hierarchically-defined surface sub-discretization. For the case of adhesive contact between powder grains in low stress regimes, this technique can allow a variety of existing contact laws to be resolved across scales, allowing for moments and torques about the contact area as well as normal and tangential tractions to be resolved. This is especially useful for multi-body simulation applications where the modeler desires statistical distributions and calibration for parameters in contact laws commonly used for resolving near-surface contact mechanics. The approach is verified against analytical results for the case of rough, elastic spheres.

**1. Introduction:**

A variety of contact laws are available in the literature to describe a wide range of contact phenomena at a similarly wide range of resolutions and assumptions. The appropriateness of particular contact laws in multi-body methods, such as discrete element modeling (DEM), is highly dependent on the application of interest. For instance, in highly dynamic ball-milling applications where the engineering property of interest is power draw, the solution is often insensitive to both form and magnitude of the elastic part of the contact law; however, the resolution of energy dissipated in contact (plastic deformation) and crushing (comminution) must be captured accurately to arrive at a useful answer. Conversely, for wave propagation studies in the elastic region, the form and magnitude of the elastic part of the contact law must be finely resolved, whereas

fracture and plastic deformation (and the associated energy loss) are unnecessary. In systems where there is high stress, and extensive plastic deformation occurs, or where the loading rate is high (e.g., shock loading of granular material), the assumptions of traditional DEM approaches are violated altogether. Certain phenomena, such as energy lost to acoustic waves dissipating energy within individual grains, can be neglected in traditional DEM models, since at the loading rates where the small deformation assumption applies, acoustic loss contributes less than 1% of the total lost energy [6]. There are limitations to using traditional DEM for capturing grain crushing and fracture; however, several approaches have been adopted to handle the case of fracturing grains, including bonded agglomerates [7], finite element sub-discretization of grains [8, 9], and statistical breakage criteria [10]. For systems of highly adhesive powders at relatively low stresses, where large plastic deformation and comminution of the grains are unlikely, inertial effects are slight, and contact properties, including coupled motions and spatially-varying attractive potentials, control the behavior of the system, it is important to adequately resolve the contact surface. This last case is the focus of this paper.

Many implementations of the DEM rely on calibrations of simple visco-elastic force-displacement relations (i.e., spring-dashpot) to model the response of materials; however, it has generally been realized that more appropriate, physically-based contact relations exist. The Hertzian solution for perfectly elastic spheres [11] is, therefore, often used to resolve the normal component of mechanical force for contacts in the absence of adhesion. Finite element codes have aided in extending the analytical forms and linearizing the results for efficient use in DEM [12]. Extensions by Mindlin [2, 3] and simplifications by others [13] are often used to capture tangential response. Other tangential force models have been proposed [14], which are validated against elasto-plastic finite element calculations. Simulations validated against experiments of oblique impact of elastic spheres [15], though, indicate that simple Hertz-Mindlin-Deresiewicz (HMD) contact [3] is insufficient to describe the complex coupling between the different degrees-of-freedom mobilized at the contact. Further evidence of non-elastic behavior in tangential loading despite elastic loading in the normal direction suggests a more complicated form to tangential force-displacement as well [16].

The extension of mechanical response to include adhesive forces has also been examined, and often the models of Johnson, Kendall, and Roberts (JKR) [4]; Derjaguin et. al (DMT) [5]; Maugis-Pollock [17]; and Maugis-Dugdale [18], which, taken together, can describe the deformation regime across the range from fully elastic to fully plastic, are used. None of these explicitly describes the mechanical response for coupled motions mobilizing multiple degrees-of-freedom but rather rely on isotropic, symmetric contact loading. Thornton and Yin [15] address adhesive contact using the JKR model and the work of Savkor and Briggs [19] to capture combined normal and tangential loading of adhesive elastic solids, offering coupling between two degrees-of-freedom. Lüding [20] proposes an adhesive elasto-plastic relation to capture adhesion effects also with tangential and normal loading; the approach is similar to an extension of the latching spring model [12] applied to adhesion with additional softening in the compressive relaxation. Recent work by Tomas [21, 22] has provided an appropriate resolution of traction resulting from mobilized frictional contact torques between idealized spherical bodies in the presence of

adhesion. All of these models, however, assume smooth surfaces, which limits the range of application.

Perfectly spherical bodies are useful in validating the assumptions of different contact laws; however, many real materials are not perfectly spherical and display shape factors that vary significantly from unity. Even small inhomogeneities in the geometry can provide significant resistance to rotation through dilation, which spheres cannot exhibit [23], or through both strong and weak geometric interlocking, a specific example of which is demonstrated by Favier [24] for ellipsoids versus ellipsoidal agglomerates of spheres. Several ad hoc approaches have been proposed to calibrate a rotational resistance term for disk- and sphere-shaped bodies [25, 26]; however, it is often desired to have a physically-motivated law rather than a purely calibrated factor. Several models instead use non-spherical, smooth bodies in 2D [27, 28] and 3D [29-34] to more closely capture the geometric interlocking between grain of engineering interest. An appropriate elasto-plastic law is further used to describe the rolling friction due to the torque associated with elastic unloading of the plastically deformed region being released coupled with the reactive force from plastic deformation at the load front .

Further complexities are introduced when not only does the shape deviate from spherical but also when there is surface roughness and angularity. The discussions of rough surface modeling for adhesive surfaces are often focused on applications to normal force resolution and are often predicated on the model of Greenwood and Williamson [35] and Greenwood and Tripp [36], models which assume that the asperity heights are statistically distributed, the asperity curvature is constant, there is no coupling between asperity deformations, and there is no bulk deformation. Recent work by Ciavarella [37] has attempted to relax the last two assumptions of the Greenwood and Williamson [35] model by proposing a discretized surface profile of the asperity peaks based on experimentally-determined surface scans and then using Hertzian contact to aggregate an effective constitutive model of the contact law for forces normal to the surface. Majumdar [38] has also presented a comprehensive theory of normal contact between rough surfaces based on accurate characterization of the fractal parameters of the roughness combined with an analytical solution of the governing mechanics.

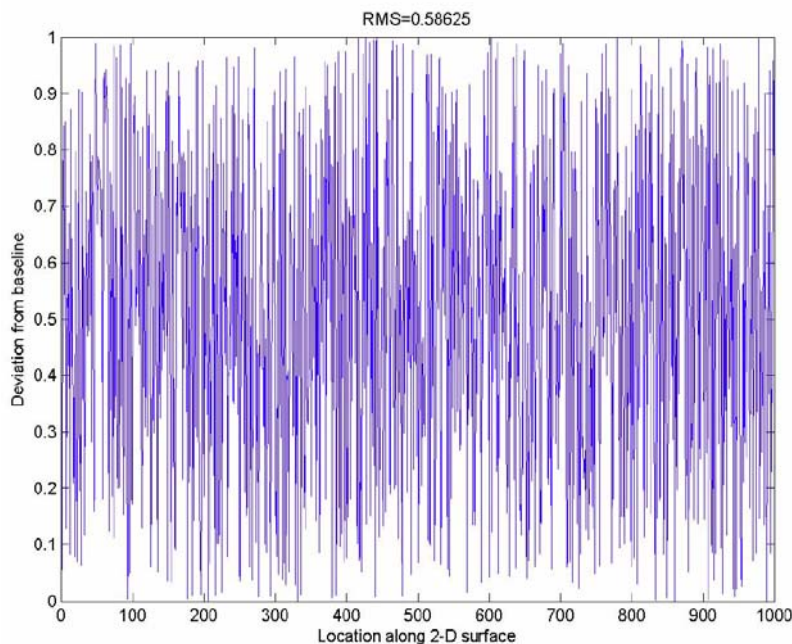
Attempts have also been made to characterize tangential surface tractions for adhesive rough surfaces, using statistically-defined surface asperity distributions. The model of Chang et. al. [39], for instance, uses an elastic perfectly brittle model to calculate tangential traction on a multi-asperity surface. Using the single asperity contact model of Hurtado and Kim [40, 41], a popular contact model for single asperity contacts, and the DMT [5] model of adhesion, Adams et. al. [42, 43] provide a physically-based, multi-asperity model of friction using an elasto-plastic model of the asperities. However, these have yet to be incorporated into memory-dependent contact algorithms for use in multi-body simulation or to handle more complex coupled motions.

Here we attempt to use a novel approach to represent multi-asperity contacts in multi-body dynamics, which allows for coupling of the surface asperities and bulk deformation when the plastic limit of the surface asperities is exceeded, a necessary extension over the model of Greenwood and Williamson [35] to capture the behaviors of interest here. This

applies to normal, tangential, twisting, and coupled motions. We achieve this by combining concepts of pixilation of the surface of individual grains with statistical distributions of asperities as well as an elasto-plastic relation for the deformation of individual asperities. The asperity state variables can be efficiently tracked over time through the use of a contact spot discretization. Generation of the contact spot properties is aided by an approach to sub-discretizing the grain surface, which was first discussed by Johnson [44, 45] and significantly extended here. The approach is also currently being extended to use other models of asperity deformation to better capture the contact physics for low-stress, adhesive contact. Though this approach has significant applications in addressing several shortcomings of many contact model implementations in multi-body physics codes by capturing the full complement of coupled-degree-of-freedom effects (at the expense of computational efficiency), the approach also has obvious extensions to many other surface phenomena of interest, such as roughness effects (with fine control of asperity scales) in aspherical soil compression; the triboelectric creation and interaction of localized electrostatic charge spots; and the bridging, ion transport, and surface charge-coupled effects of adsorbed water and other volatile compounds.

## 2. Drawbacks of Typical Surface Morphology Characterization Metrics:

The determination of when an angular deviation should be considered as part of the general topology (sphericity term) or when a small asperity should be included with the angularity term is currently subjective, though, objective measures have been established to try to address this. Even with objective metrics, the classifications are dependent on the application. It can be readily seen that an asperity of 1% the height of the smallest dimension of the particle may be included in the friction parameters (roughness) for a compressed dense fabric analysis, but that same asperity may need to be explicitly modeled if the particle is being measured for the rebound angle after collision.



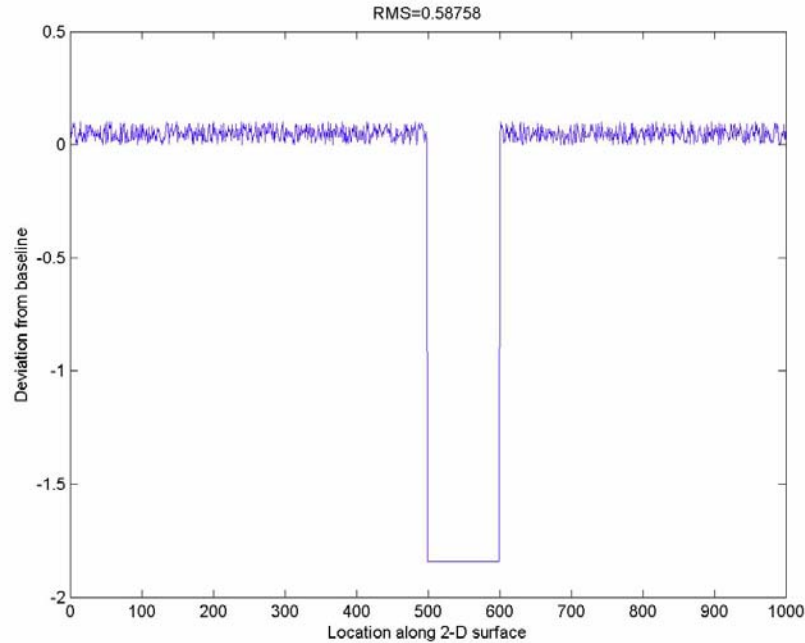


**Figure 1: Illustration of similar RMS values for dissimilar surface profiles**

Systematic methods to characterize material shape quantitatively have received greater attention over the previous decade. For powder characterization, a coarse convex geometry is generally assumed and asperities are then characterized by statistical relations based on the deviation of the surface from the coarse approximation. Commonly used metrics are the root mean square (RMS) deviations of the surface [46] based on the finest observed resolution data. This uses the first moment of the distribution (the variance) of the asperities. The mean as well as higher order moments (skewness and kurtosis) are also sometimes used to characterize a surface [46]. The drawback to this type of analysis is the loss of potentially important information. For instance, as Figure 1 shows, the most common measure, RMS, will yield a metric that has the same result for a smooth surface with a few large asperities (bottom) as a rougher surface of smaller asperities (top). For contact mechanics and interaction force theories, these two types of surfaces yield drastically different behavior. A similar effect was theorized by Sayles [47], and it was shown that stochastic surface profiles are sensitive to the scanning length (analysis window) and the frequency. The shortcomings in these models, therefore, lie in the inability to capture particle morphology across a range of scales. Relatively recently, self-similar fractal surfaces have been assumed and confirmed for many engineering surfaces of interest [35, 38, 48], and it is the measurement of these parameters that are key.

Despite the realization among theoreticians that fractal geometry describes roughness well, in practice there is often a lack of a common framework to measure particle morphology and differing resolution requirements between different applications, which has generally led to the adoption of the coarsest model by those designing multi-body simulations to determine the emergent behavior of large numbers of interacting rough bodies. For instance Odagi [49] uses a mono-disperse distribution of hemispherical

asperities to model surface angularity, which disregards the multi-scale nature of surfaces. It should be noted that the concept used by Odagi [49] was first forwarded by Archard [50, 51] as a multi-scale description of surface asperities; however, this model has yet to be incorporated into multi-body simulations. Most importantly, because the most successful models of rough contact described earlier are based on statistical descriptions of surfaces and contacting surfaces are often characterized by only a few hundred contacting asperities [52], it is unclear how these models can be directly applied to multi-body simulations at the grain-scale, since the phenomenology at the length scale being modeled will be affected by the stochastic variability of the involved contacts.

The confounding problem seems to be that geometric features are not separable into distinct categories but are continuous across scale as discussed earlier. A proper framework would integrate the property of continuity across scale to allow descriptions of roughness and the resultant mechanical behavior from roughness. From this logic, it would be preferable to have a hierarchical computational method for describing particle geometry, allowing the modeler to only include shape resolution to the depth necessary for the problem, as suggested by the band-pass model of Thomas and Sayles [53].

The ability to model object resolution in a hierarchical framework is not necessarily a new idea. Demand from 3-D game design, recent interest in agent-based computing/visualization, and scientific visualization research have advanced the study of hierarchical geometric representations over the past decade. These have included increased refinement of voxelization [54], spherical harmonics [55], radial basis functions [56], and surface wavelets. For roughly spherical particles, for instance, spherical wavelets [57] can be used to capture hierarchically more detailed resolutions of a general topology with specific application to graphical texture mapping.

Though excellent at representing geometries efficiently for graphics rendering, this work had generally been poor at capturing surface normals and edge features that are fundamental to accurately resolving contact in particle methods, such as discrete element modeling. As an extension of the work in computer graphics, researchers adapted some of these methods for characterizing real-world granular materials. The idea of using spherical harmonics for capturing particle shape in a hierarchical manner was forwarded by Garboczi [55]. A more general method of capturing surface morphology using surface wavelets was formulated in the context of discrete element modeling by Williams and Amaratunga [58] and further developed for general surface integral evaluations by Amaratunga [59, 60].

These approaches are excellent for categorization of particles and provide a more precise characterization of granular materials over the classic categories of sphericity, angularity, and roughness. They also have the flexibility of capturing surface normals required for resolving contact. However, these hierarchical approaches have a drawback for application in DEM, in that the generality of the methods disregards the existence of an implicit convex hull for the geometry, and it is not obvious how to efficiently calculate properties necessary to resolve contact between adjacent bodies. Simple convex hulls are a key requirement for a contact detection algorithm in DEM to work efficiently. By applying destructive geometry to a simple gross topology, wavelets could theoretically be



used to characterize the angularity and roughness that describes the difference between a particle and the simple primitive used to approximate it, though, this has yet to be implemented. In this paper, we propose a simpler model using nested surface maps, which allows both hierarchically defined surface properties as well as a fast and efficient value query.

### 3. Surface Representation of the Grain:

The ability to layer information on the surface of a body can be useful from several different viewpoints. Layering of data for surface properties is achieved through a procedure akin to texture mapping in computer graphics. A 2-D patch is mapped over the surface of a convex body using a curvilinear (U-V) coordinate system corresponding to local latitudes and longitudes on the particle surface. For ease of reference, the procedure developed here will be called the surface discretization model (SDM) throughout the paper.

Any number of scalar and vector data can be layered onto a geometric primitive in this way. If the data being layered is, for instance, asperity height data, it can be represented in the map much like digital elevation map data on a regular grid, except the baseline is the geometric boundary of the primitive and the height data represents the depth of indentations on the surface, allowing the primitive to become a convex hull. Roughness can be defined in terms of the unsigned deviation of the true radius from the gross geometry assumed. The deviation will be taken as unsigned so as to enforce the constraint that the gross geometry be a convex hull of the particle, which is amenable to use in contact resolution schemes.

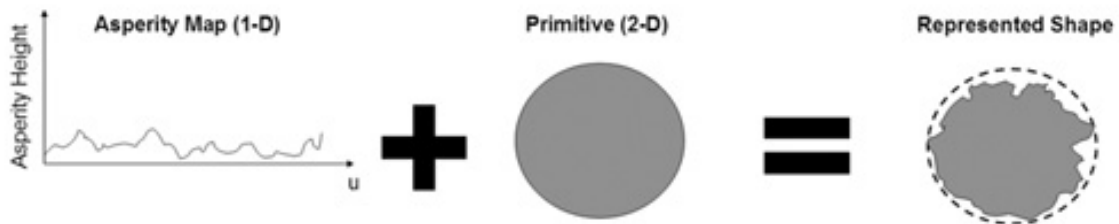


Figure 2: Illustration of data layering for a 1-D map and 2-D primitive: an unsigned 1-D function is used to map multi-physics information (e.g., asperity depth data) onto the surface

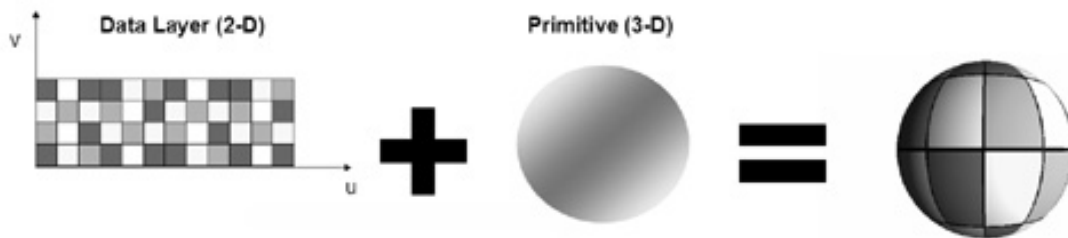


Figure 3: Illustration of data layering for a 2-D map and 3-D primitive: an unsigned 2-D function is used to map asperity depth data onto the surface.

In Figure 2, the data layering approach that will be described in this section is used to capture asperities. The example in Figure 2 is in 2-D to illustrate the details of applying the method; however, the extension to 3-D naturally follows as shown in Figure 3.

The map is created using an array of dimension 3, where the dimensional discretization is of size  $[num_u, num_v, num_p]$ .  $num_u$  indicates the discretization along the latitudinal direction,  $num_v$  the discretization along the longitudinal direction, and  $num_p$  indicates the number of layers of information (extra parameters) being modeled. For instance, a map containing a scalar characterizing surface water adsorption, a local surface energy scalar, and asperity height data would be  $num_p=3$ .

To map a point in the global reference frame to the map, which is based in the local reference frame of the body of interest, the following procedure may be used.

$$\begin{aligned}\vec{c}_{global} &= \vec{cp} - \vec{cog} \\ \vec{c}_{local} &= R \cdot \vec{c}_{global} \\ \vec{c}_{normal} &= \frac{\vec{c}_{local}}{|\vec{c}_{local}|} \\ \phi &= \cos^{-1}(\vec{c}_{normal} \cdot \hat{k})\end{aligned}$$

**EQ 1**

where  $\vec{cp}$  is the global coordinate of the point,  $\vec{cog}$  is the centroid of the particle, and  $R$  is the rotation tensor.

If  $\sin(\phi)=0$ , then  $\theta=0$ . Otherwise, the  $\theta$  angle is determined through the following procedure:

$$\begin{aligned}
\vec{c}_{normal,ij} &= \frac{(\vec{c}_{normal} \cdot \hat{i}) \cdot \hat{i} + (\vec{c}_{normal} \cdot \hat{j}) \cdot \hat{j}}{[(\vec{c}_{normal} \cdot \hat{i}) \cdot \hat{i} + (\vec{c}_{normal} \cdot \hat{j}) \cdot \hat{j}]} \\
v_1 &= \text{sign} \left( \frac{\vec{c}_{normal,ij} \cdot \hat{i}}{\sin(\phi)} \right) \\
v_2 &= \text{sign} \left( \frac{\vec{c}_{normal,ij} \cdot \hat{j}}{\sin(\phi)} \right) \\
\theta_1 &= \left| \cos^{-1} \left( \frac{\vec{c}_{normal,ij} \cdot \hat{i}}{\sin(\phi)} \right) \right| \\
\theta_2 &= \begin{cases} 0, & v_1 > 0, v_2 \geq 0 \\ \pi/2, & v_1 \leq 0, v_2 > 0 \\ \pi, & v_1 < 0, v_2 \leq 0 \\ 3\pi/2, & v_1 \geq 0, v_2 < 0 \end{cases} \\
\theta &= \theta_1 + \theta_2
\end{aligned}$$

EQ 2

Note that the variables  $\theta$  and  $\phi$  are constrained to be in:

$$\begin{aligned}
0 &\leq \theta < 2\pi \\
0 &\leq \phi < \pi
\end{aligned}$$

For a map of size  $[num_u, num_v]$ , the bins corresponding to the point  $\vec{cp}$  can then be found as:

$$\begin{aligned}
bin_u &= \text{floor} \left( num_u \frac{\theta}{2\pi} \right) \\
bin_v &= \text{floor} \left( num_v \frac{\phi}{\pi} \right)
\end{aligned}$$

EQ 3

If the data layer, for example, holds asperity height data, simply scale the value in  $map[bin_u, bin_v]$  appropriately and subtract it from the calculated normal at point  $\vec{cp}$ . Note that  $map[bin_u, bin_v]$  denotes the value of the data layer array corresponding to  $(bin_u, bin_v)$ . This general procedure can be used for any scalar data:

$$\rho_{perturbed} = \rho_{unperturbed} - \beta_0 \cdot map[bin_u, bin_v]$$

EQ 4

where  $\beta_0$  is the scaling factor at level 0.

For a smoothed value of the scalar, a simple linear shape function interpolation can be used by assuming that the scalar value represented by the cell is centered in the cell:

$$\delta_u = 2 \cdot \left( num_u \frac{\theta}{2\pi} - bin_u - 0.5 \right) \quad \text{EQ 5}$$

$$\delta_v = 2 \cdot \left( num_v \frac{\phi}{\pi} - bin_v - 0.5 \right) \quad \text{EQ 6}$$

$$\rho_u = \begin{cases} |\delta_u| \text{map}[bin_u, bin_v] + (1 - |\delta_u|) \text{map}[bin_u - 1, bin_v] & , \quad bin_u > 0, \delta_u \leq 0 \\ |\delta_u| \text{map}[bin_u, bin_v] + (1 - |\delta_u|) \text{map}[bin_u + 1, bin_v] & , \quad bin_u < num_u - 1, \delta_u > 0 \\ |\delta_u| \text{map}[bin_u, bin_v] + (1 - |\delta_u|) \text{map}[num_u - 1, bin_v] & , \quad bin_u = 0, \delta_u \leq 0 \\ |\delta_u| \text{map}[bin_u, bin_v] + (1 - |\delta_u|) \text{map}[0, bin_v] & , \quad bin_u = num_u - 1, \delta_u > 0 \end{cases} \quad \text{EQ 7}$$

$$\rho_v = \begin{cases} |\delta_v| \text{map}[bin_u, bin_v] + (1 - |\delta_v|) \text{map}[bin_u, bin_v - 1] & , \quad bin_v > 0, \delta_v \leq 0 \\ |\delta_v| \text{map}[bin_u, bin_v] + (1 - |\delta_v|) \text{map}[bin_u, bin_v + 1] & , \quad bin_v < num_v - 1, \delta_v > 0 \\ \text{map}[bin_u, bin_v] & , \quad bin_v = 0 \mid bin_v = num_v - 1, \delta_v \leq 0 \end{cases} \quad \text{EQ 8}$$

$$\tilde{\rho} = \frac{(|\delta_u| \rho_u + |\delta_v| \rho_v)}{\sqrt{(\delta_u^2 + \delta_v^2)}} \quad \text{EQ 9}$$

The further capability of this method comes from its extension across multiple scales. The simplest method of extension is by subdividing each grid cell into a new grid of  $num_u \times num_v$  cells. The part of the contact point  $\vec{cp}$  resolved at level  $n-1$  is removed for the analysis at level  $n$ , and the remainder is mapped onto the data layer and scaled by  $\beta_i$  where  $i=[0,n]$ . The general concept is illustrated in Figure 4.

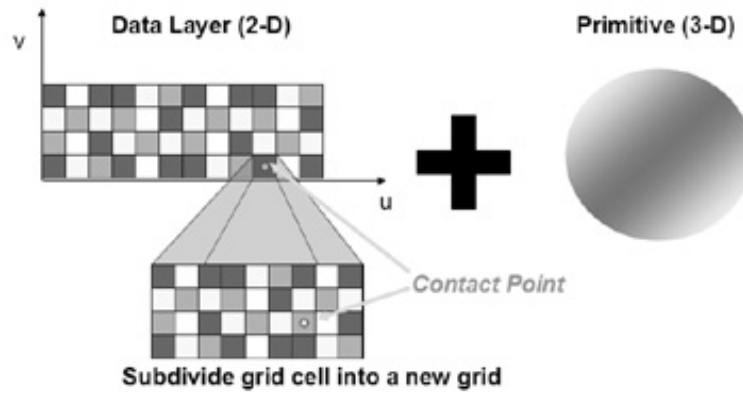


Figure 4: Illustration of grid subdivision for a 3-D primitive.

The component of  $\theta$  and  $\phi$  at level  $n-1$  can be determined by the following equations:

$$\theta_i = 2\pi \sum \left( \frac{bin_{u,i}}{num_u^{i+1}} \right)$$

$$\phi_i = \pi \sum \left( \frac{bin_{v,i}}{num_v^{i+1}} \right)$$

**EQ 10**

where  $\theta_i = \phi_i = 0$  when  $i < 0$ .

The mapped bins corresponding to these values can then be determined by:

$$bin_{u,i} = num_u^{i+1} \frac{\theta - \theta_{i-1}}{2\pi}$$

$$bin_{v,i} = num_v^{i+1} \frac{\phi - \phi_{i-1}}{\pi}$$

**EQ 11**

The scaled scalar is then calculated:

$$\tilde{\rho}_i = \beta_i \cdot map[bin_{u,i}, bin_{v,i}]$$

**EQ 12**

where  $map[bin_{u,i}, bin_{v,i}]$  is the scalar associated with  $bin_{u,i}$  and  $bin_{v,i}$ ,  $\beta_i$  is the scale factor associated with the map hierarchy level  $i$ , and  $\tilde{\rho}_i$  is the final scaled value of the scalar for level  $i$ .

As an example of the application of the multi-scale procedure, assume that the map is a 2x2 map along  $\theta=[0,2\pi)$  and  $\phi=[0,\pi)$ , the point to be mapped lies in the local reference frame at  $\theta=3\pi/2+0.1$  and  $\phi=\pi/2+0.2$ , and the map is a 2 level hierarchy with the scaling factor  $\beta_i=\beta_{i-1}/2$ . The 2x2 map is specified as:

$$map = \begin{bmatrix} -1 & 1 \\ -1 & 1 \end{bmatrix}$$

The procedure would be applied as follows, using EQ 10- EQ 12:

First level:

$$bin_{u,0} = floor\left(2 \frac{3\pi/2 + 0.1 - 0}{2\pi}\right) = 1$$

$$bin_{v,0} = floor\left(2 \frac{\pi/2 + 0.2 - 0}{\pi}\right) = 1$$

$$\theta_0 = 2\pi\left(\frac{1}{2}\right) = \pi$$

$$\phi_0 = \pi\left(\frac{1}{2}\right) = \frac{\pi}{2}$$

Second level:

$$bin_{u,1} = floor\left(4 \frac{3\pi/2 + 0.1 - \pi}{2\pi}\right) = 1$$

$$bin_{v,1} = floor\left(4 \frac{\pi/2 + 0.2 - \pi/2}{\pi}\right) = 0$$

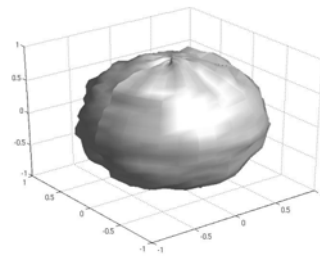
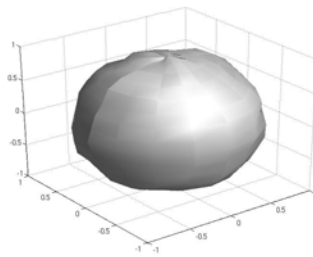
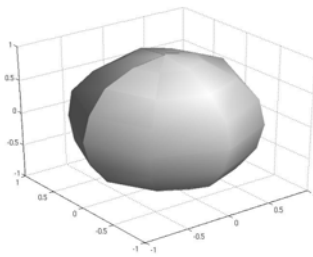
$$\theta_1 = 2\pi\left(\frac{1}{2} + \frac{1}{4}\right) = \frac{3\pi}{2}$$

$$\phi_1 = \pi\left(\frac{1}{2} + \frac{0}{4}\right) = \frac{\pi}{2}$$

Note that at level 1,  $\theta_1 = 3\pi/2 = \theta \cdot R$  where the residual  $R=0.1$ , and  $\phi_1 = \pi/2 = \phi \cdot R$  where the residual  $R=0.2$ .

To acquire the multiscale reconstruction of the map value, take:

$$\begin{aligned} \sum (\beta_i \cdot map_i) &= \beta_0 \cdot map[1,1] + \beta_1 \cdot map[1,0] \\ &= 1 \cdot 1 + 0.5 \cdot 1 = 1.5 \end{aligned}$$



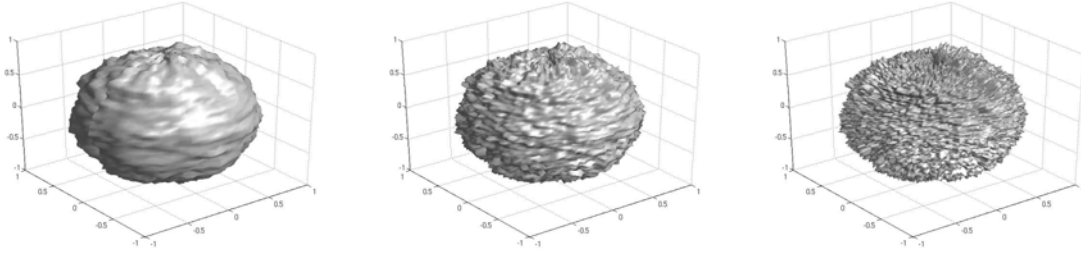


**Figure 5: Illustration of hierarchical destructive geometry representation of surface profiles for (from top left to lower right) levels 0-5 of refinement**

An example is visualized in Figure 5 for scalar surface profile information where the number of bins is 8 in each direction ( $u$  and  $v$ ) for the parent map (0-level) and 2 in each direction for each higher level map. The radius deviations are sampled from a uniform random distribution in the range  $[0,1]$  with a constant scale factor of 5% applied, so the effective distribution is uniform random in the range  $[0,0.05]$ .

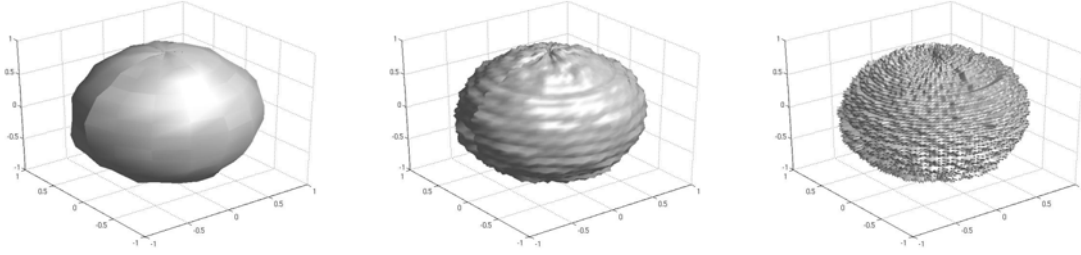


**Figure 6: Illustration of self-similar hierarchical representation for (left to right) levels 1-3 of refinement**

Because the subdivision can result in a self-similar grid (i.e., a fractal material), the memory required to capture an infinite number of details for a self-similar material for all of the particles in a system can be as little as  $O(num_u num_v)$ . This is possible because a reference to the map can be applied to each particle in the system and only one data structure need be stored. As an illustration, taking an original  $4 \times 4$  map populated from samples in a random uniform distribution in the range  $[0,0.05]$ , provides the result shown in Figure 6 when applied in a self-similar grid hierarchy.

#### 4. Surface Representation of the Contact:

The SDM can be used to represent a variety of surface-based properties. If we use the SDM to represent unsigned deviations of the actual surface profile from the assumed convex hull (e.g., a sphere), we can acquire the average deviation of the surface profile for the scale defined at level  $N-1$  and the contact spot, a mesh representing the local area around the contact, at level  $N$ . An exaggerated example of the representation at level  $N-1$  is illustrated in Figure 7. Though it is possible for this geometry specification to result in multiple points of contact on different points at level  $N-1$ , this is not captured in this model, though, multi-point contacts of the asperities (at level  $N$ ) are. That is, only surface torques due to asperity contacts in a single local region of contact are resolved.

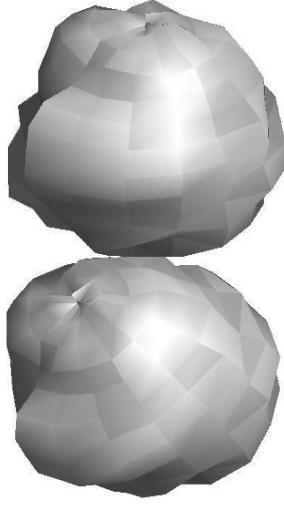


**Figure 7: Coarsely approximated irregular bodies in contact**

Using the approach described in the previous section (EQ 1-EQ 4 and optionally EQ 5-EQ 9), the scalar value at the point of contact can then be acquired (at level  $N-1$ ); this can be used to provide the base depth for a statistical distribution of asperity depths at level  $N$ . Level  $N$  is assumed here to be the level of resolution of the same length scale as the potential contact spot. Together, the generated incremental asperity depth profile at level  $N$  can be combined with the perturbed radius (from the hierarchical representation through level  $N-1$ ) to populate a contact spot discretization (CSD):

$$r_{profile}(u, v) = r_{perturbed} - X(u, v)$$

**EQ 13**

where  $r_{profile}(u, v)$  is the surface profile along the contact spot (where the spot is described by the orthogonal parameters  $u$  and  $v$ ),  $r_{perturbed}$  is the output of EQ 4, and  $X(u, v)$  is an arbitrary unsigned function describing the additional asperity depth.  $X(u, v)$  may be any arbitrary form, including a simple statistical distribution, a distribution with complicated autocorrelations, or a function derived from an AFM scan of an actual surface.



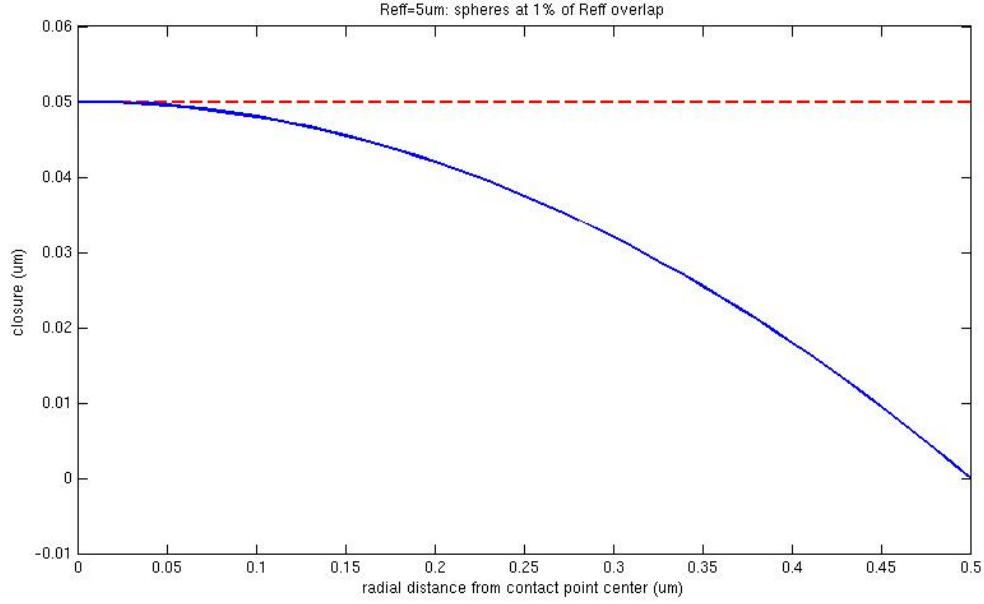


**Figure 8: Closure of surfaces of 10um spheres for surfaces assumed locally planar vs locally spherical**

A further correction of the surface profile, though, needs to be applied to adjust for the finite curvature of the surface. For a 100nm overlap on a 20μm spherical powder grain, the maximum geometric error (at the contact edge) is approximately 500Å (well beyond the point at which surfaces are assumed in contact), as is illustrated in the plot of closure in Figure 8 for a surface assumed locally planar versus one in which the surface is assumed to be spherical.

Without correction, the surface would appear to be in closer compliance than in the modeled system, the contact torques are overestimated, which is generalizable to any convex surface, providing an artificial van der Waals stiffening at the edges of the adhesive contact. For the special case of a sphere, a correction factor can be formulated as follows:

Let  $u$  and  $v$  denote the orthogonal parameters of the common plane of contact and  $y$  denote the parameter in the direction normal to the common plane of contact towards the surface of the sphere denoted by the subscript  $I$ ; then the correction to the closure,  $c[u, v]$ , of the surface in terms of the common plane coordinates can be given by:

$$c[u, v] = y_0(x_u, x_v) - y_1(x_u, x_v) \quad \text{EQ 14}$$

$$y_0(x_u, x_v) = \sqrt{R_0^2 - x_u^2 - x_v^2} \quad \text{EQ 15}$$

$$y_1(x_u, x_v) = R_0 + R_1 - \alpha - \sqrt{R_1^2 - x_u^2 - x_v^2} \quad \text{EQ 16}$$

$$x_u = \delta_u \left( \frac{u}{num_u} - 0.5 \right)$$

EQ 17

$$x_v = \delta_v \left( \frac{v}{num_v} - 0.5 \right)$$

EQ 18

where  $\delta_u$  is the length of the contact spot discretization in the  $u$ -direction, and  $\delta_v$  is the length of the contact spot discretization in the  $v$ -direction.

Further corrections must be made as the contact evolves in time both by translating and rotating. The goal is to maintain the center of the contact spot at the point of contact as it evolves in time. The matching of surfaces between potentially contacting bodies is performed through a procedure discussed later, leaving only the issue of how to update the discretization of the contact spot efficiently as it traverses the surface.

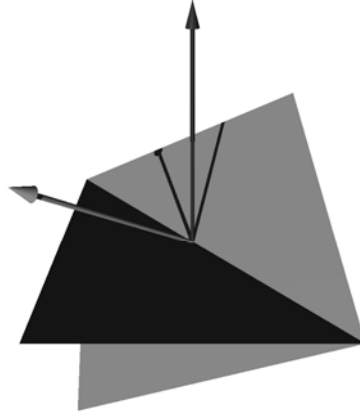


**Figure 9: Visualization of plane rotated about 2 degrees of freedom, excluding rotation about the normal direction**

Because relative rotation about the surface normal is handled during the step of resolving contact spot mesh interaction between the interacting bodies, any arbitrary rotation that satisfies the mapping to the new common plane between the bodies can be adopted. Thus, the most natural and simplest transformation is to constrain rotation about the surface normal, allowing a simple linear gradient to transform the scalar values into the new transformed coordinates. A specific case of this constraint is shown in Figure 9. The following relations can be used to transform the old scalar values into the new coordinate system for the rotated point:

$$\hat{s}_\tau = \frac{\hat{t}_{\tau-1} \times \hat{n}_\tau}{|\hat{t}_{\tau-1} \times \hat{n}_\tau|}$$

EQ 19

$$\hat{t}_\tau = \frac{\hat{n}_\tau \times \hat{s}_\tau}{|\hat{n}_\tau \times \hat{s}_\tau|} \quad \text{EQ 20}$$

$$\vec{x}_\tau = \vec{x}_{\tau-1} + \left( \left( \overrightarrow{cp_\tau} - \vec{x}_{\tau-1} \right) \cdot \hat{n}_\tau \right) \hat{n}_\tau \quad \text{EQ 21}$$

$$\vec{\delta}_\tau = \left( \left( \vec{x}_\tau - \overrightarrow{cp_\tau} \right) \cdot \hat{s}_\tau \right) \hat{s}_\tau + \left( \left( \vec{x}_\tau - \overrightarrow{cp_\tau} \right) \cdot \hat{t}_\tau \right) \hat{t}_\tau \quad \text{EQ 22}$$

$$map[u, v]_\tau = map[u, v]_{\tau-1} + \left( \frac{u\delta_u}{num_u} \hat{s}_{\tau-1} + \frac{v\delta_v}{num_v} \hat{t}_{\tau-1} + \left( \overrightarrow{cp_\tau} - 2\vec{x}_{\tau-1} \right) \right) \cdot \hat{n}_\tau \quad \text{EQ 23}$$

where  $\hat{s}_\tau$  is the director in the  $s$ -parameter direction at time  $\tau$ ,  $\hat{t}_\tau$  is the director for the  $t$ -parameter direction at time  $\tau$ ,  $\vec{x}_\tau$  is the centroid of the contact spot at time  $\tau$ ,  $\vec{\delta}_\tau$  is the difference between the position of the contact point at time  $\tau$  and the position of the centroid of the contact spot at time  $\tau$ , and  $map[u, v]_\tau$  is the new value of the scalar in the cell addressed as  $[u, v]$  at time  $\tau$ . The sum on the last parenthetical term is correct (rather than a difference), since the  $map$  values represent depths rather than asperities. The frame of reference can also be in either the global (inertial) or local (convective) frame as long as the convention is adopted consistently.

For translation, a “conveyer belt” approach is used where  $map$  used to define the contact spot is kept at a constant matrix size, but cells are shifted as the contact point moves, and new material is “loaded” onto the approached sides. Physically, the model implies that material history associated with the material outside of the CSD footprint is lost. The translation procedure is triggered when the projection of the contact point onto the plane falls outside of 1 cell from the center; that is, whether  $\vec{\delta}_\tau$  is more than a single bin in magnitude. When triggered, all cells are shifted by the appropriate number of bins along each orthogonal direction, and  $\vec{x}_\tau$  is reset to the new center. The procedure is outlined below:

$$n_u = \begin{cases} \text{int} \left( \frac{num_u}{\delta_u} \left( \vec{x}_\tau - \overrightarrow{cp_\tau} \right) \cdot \hat{s}_\tau \right) & , \quad \left| \left( \vec{x}_\tau - \overrightarrow{cp_\tau} \right) \cdot \hat{s}_\tau \right| > \frac{\delta_u}{num_u} \\ 0 & , \quad otherwise \end{cases} \quad \text{EQ 24}$$

$$n_v = \begin{cases} \text{int} \left( \frac{num_v}{\delta_v} \left( \vec{x}_\tau - \overrightarrow{cp_\tau} \right) \cdot \hat{t}_\tau \right) & , \quad \left| \left( \vec{x}_\tau - \overrightarrow{cp_\tau} \right) \cdot \hat{t}_\tau \right| > \frac{\delta_v}{num_v} \\ 0 & , \quad otherwise \end{cases} \quad \text{EQ 25}$$

If  $\left| \left( \vec{x}_\tau - \overrightarrow{cp_\tau} \right) \cdot \hat{s}_\tau \right| > \frac{\delta_u}{num_u}$  or  $\left| \left( \vec{x}_\tau - \overrightarrow{cp_\tau} \right) \cdot \hat{t}_\tau \right| > \frac{\delta_v}{num_v}$  then

For indices in the range  $0 \leq u + n_u < num_u$  and  $0 \leq v + n_v < num_v$

$$map_{shift}[u, v]_{\tau} = map[u + n_u, v + n_v]_{\tau}$$

For indices outside of the range but where  $0 \leq u < num_u$  and  $0 \leq v < num_v$

$$map_{shift}[u, v]_{\tau} = new\_value$$

where new\_value is a new population value sampled from the original distribution used to seed the profile layer.

and

$$\vec{x}_{shift, \tau} = \vec{x}_{\tau} + n_u \frac{\delta_u}{num_u} \hat{s}_{\tau} + n_v \frac{\delta_v}{num_v} \hat{t}_{\tau}$$

**EQ 26**

The correction for the surface curvature is not included yet in the formulation of  $map_{shift}[u, v]_{\tau}$ . For implementation with arbitrary convex hull geometries, the curvature correction term should be calculated at each time step and applied. However, for the special case of spheres, the curvature is globally constant, and the curvature correction is time-invariant. This attribute combined with the procedure to maintain the contact spot's center about the contact point, allows the curvature to be cached in a data structure of the same size as the map, as described by EQ 14-EQ 18.

So far, the procedure is fairly straightforward, and its simplicity can be translated directly into efficiency. There still remains, though, the issue of resolving the relative rotation about the contact point normal to the surface. This requires combining the now coplanar regular grid meshes and determining the new closure conditions. These meshes are, unfortunately, not necessarily aligned in coordinate space, and the area of overlap will often be an irregular polygon, as shown in the example in Figure 10.

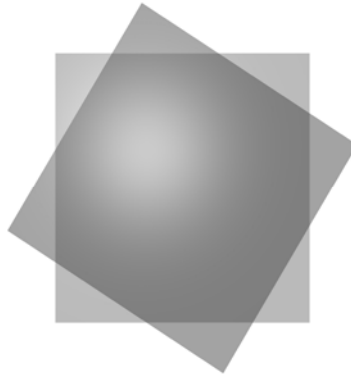


**Figure 10: Overlap of contact spot meshes from each interacting body**

To resolve the rotation about the normal to the common plane, a host surface is first chosen. Here, the surface labeled with subscript 0 is arbitrarily chosen to be the host

surface. For simplicity, the asperities are assumed to be discrete cylindrical bodies oriented along the normal with hemispherical tips. The cylindrical asperities on surface  $I$  can now be binned into the appropriate surface bins on surface  $O$ , reducing the problem to a simple 2-D neighbor-sorting problem for mono-disperse disks, which can be efficiently addressed using a number of different algorithms [61-68]. The nearest neighbor determination is used to populate a matrix in the surface  $O$  frame of reference ( $map_{remap}[u, v]_{\tau_1}$ ):

$$c_{adjusted}[u, v] = (y_0(x_u, x_v) - map_{shift}[u, v]_{\tau_0}) - (y_1(x_u, x_v) + map_{remap}[u, v]_{\tau_1}) \quad \text{EQ 27}$$

Once the nearest neighbors have been determined, the contact can be resolved using the modeler's choice of pairwise asperity contact laws.

## 5. Characterization of Normal Loading:

To verify the approach, a simple test case is investigated, where the computational asperities span the entire surface of the sphere as a thin film, such that, these computational asperities represent a perfect partitioning of the elastic surface of a sphere with no gaps or disturbances. For this simple case, the computational asperities are modeled using a serial spring model where the underlying grain body is modeled using the Hertzian [1] solution for elastic spheres with the individual asperities modeled as simple elastic columns in uniaxial compression:

$$\sum \sum \frac{E \delta_u \delta_v}{h \cdot num_u num_v} \left( c_{adjusted}[u, v] - \gamma \delta_{sphere} + \frac{1}{2R} (x_u^2 + x_v^2) \right) = \frac{4E\sqrt{R}}{3(1-\nu^2)} \gamma^{3/2} \delta_{sphere}^{3/2} \quad \text{EQ 28}$$

By substituting  $\mathcal{G} = \sqrt{\gamma}$  in EQ 28 and solving the resultant cubic equation for  $\mathcal{G}$ , the new value of  $\delta_{sphere}$  is  $\delta_{sphere}' = \mathcal{G}^2 \delta_{sphere}$ , and a convergent solution can be obtained through iteration. Convergence is assumed to be reached when:

$$\left| \sum \sum \frac{E \delta_u \delta_v}{h \cdot num_u num_v} \left( c_{adjusted}[u, v] - \gamma \delta_{sphere} + \frac{1}{2R} (x_u^2 + x_v^2) \right) - \frac{4E\sqrt{R}}{3(1-\nu^2)} \gamma^{3/2} \delta_{sphere}^{3/2} \right| < tol \quad \text{EQ 29}$$

Here we evaluate the case of quasi-static contact between a pair of similar, non-adhesive, frictionless, smooth spheres. We can assume that the map values are a constant, and the only equation required is the spherical curvature correction EQ 14. This particular case physically represents a sphere covered with a uniform height surface (30nm) of perfectly aligned and compliant asperities and can also be thought of as an elastically-deformable

sphere covered in a thin, elastic film of material with no shear strength. The asperities for this case are modeled as perfectly elastic columns of silica (73GPa Young's modulus with a Poisson's ratio of 0.16).

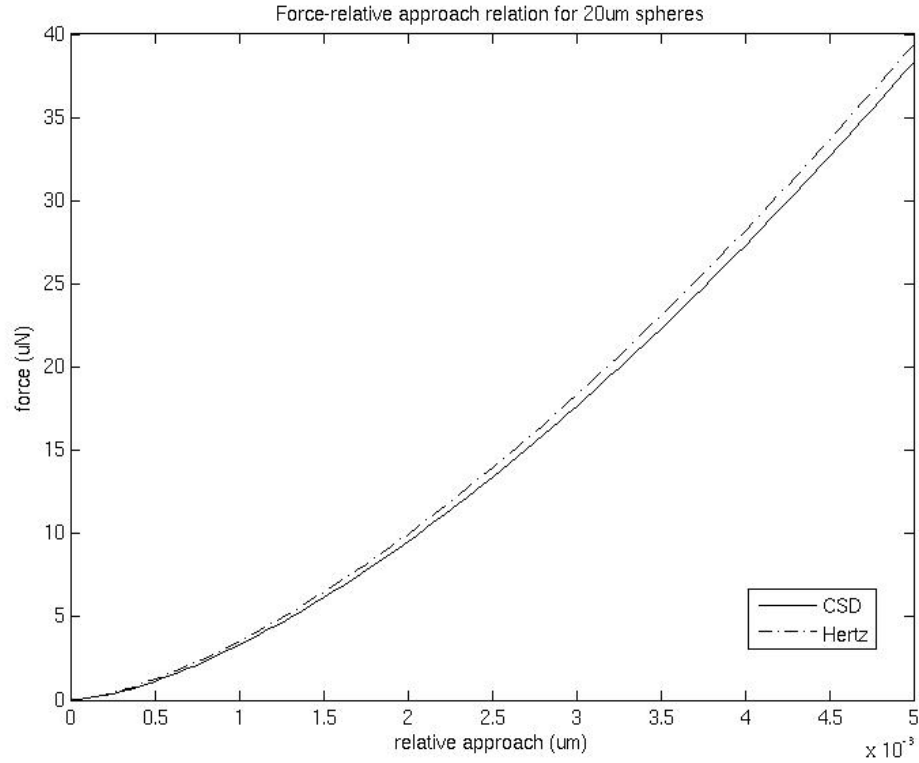


**Figure 11: Force-displacement relationship for quasi-static approach of spherical bodies in the absence of adhesion for relative approach below 50Å**

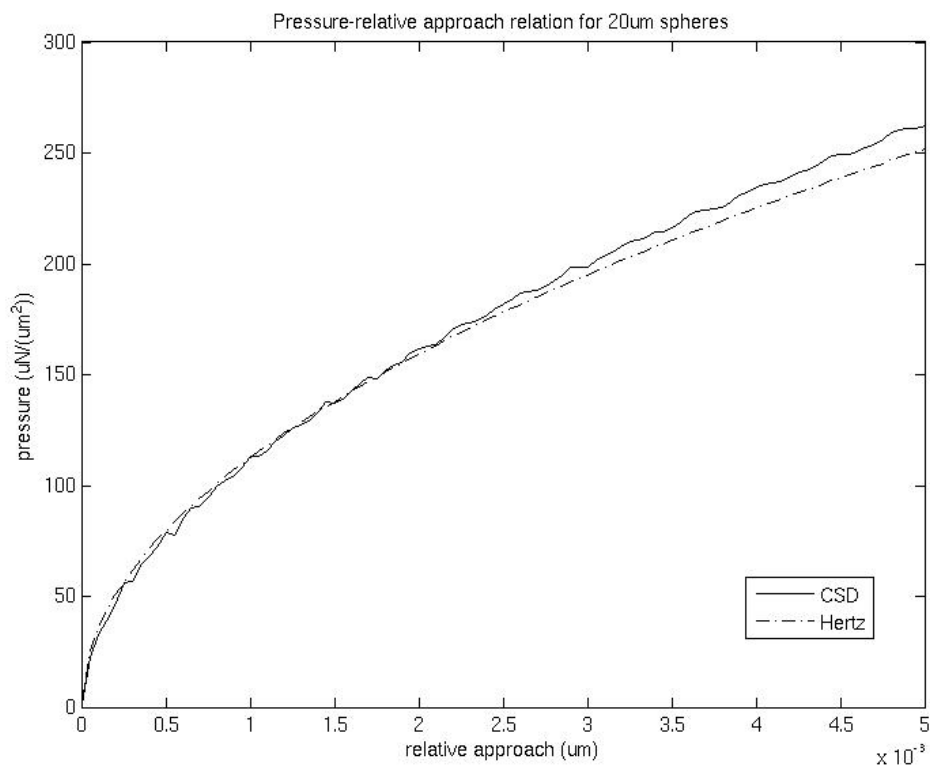


**Figure 12: Pressure-relative approach relationship for quasi-static approach of spherical bodies in the absence of adhesion for relative approach below 50 $\text{\AA}$**

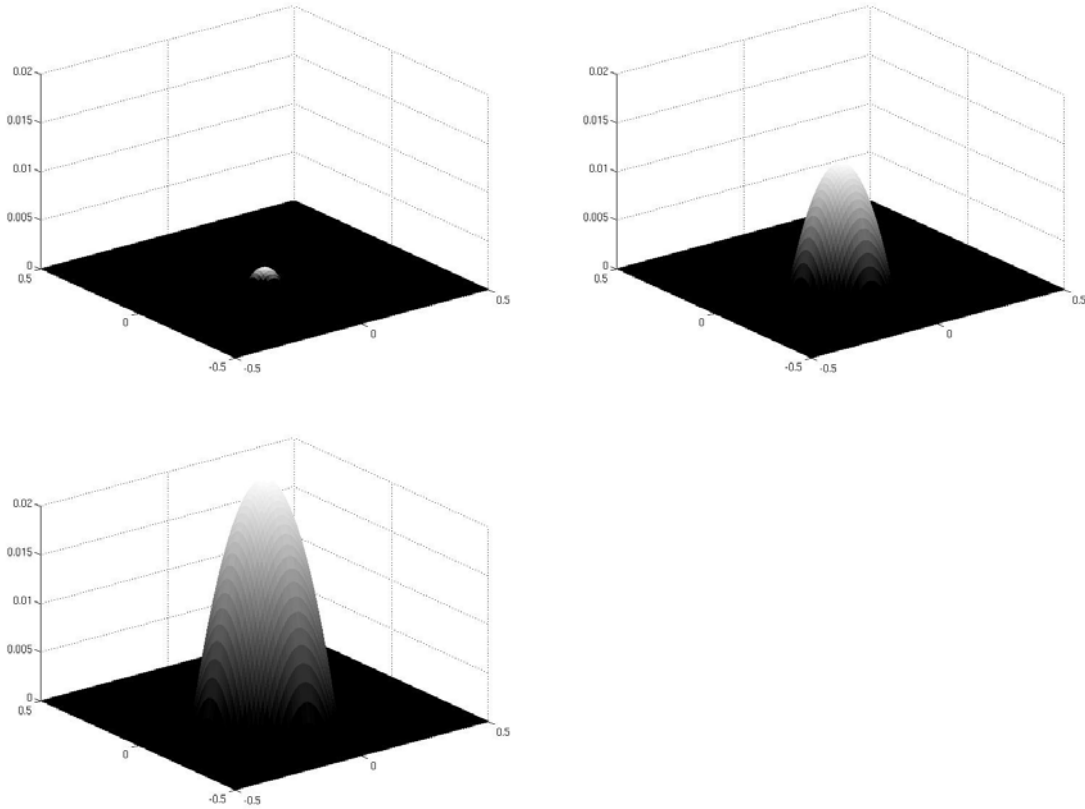


**Figure 13: Surface profiles (abscissas in  $\mu\text{m}$ ) of normal tractions (vertical axis in  $\mu\text{N}$ ) for  $20\mu\text{m}$  adhesionless, elastic spheres with uniform  $30\text{nm}$  asperities with relative approach of  $2.5\text{nm}$ ,  $25\text{nm}$ , and  $50\text{nm}$**

Figure 11 compares the Hertzian solution [1] for frictionless spheres with the CSD approach for surface roughness. The procedure can also capture the profile of surface tractions, as shown in Figure 13. As the relative approach increases the assumption of no shear strength becomes increasingly inappropriate for describing the response of the surface as can be noted from Figure 12.

## 6. Implementation of Archard's Theory:

As an illustration of the technique and a further verification of its applicability, the rough sphere model of Archard [50, 51] is implemented and compared against analytical results. We use the assumptions of Archard [51] that the radius of the asperities are small compared to the radius of the spherical body, and the general stress distribution in the spherical body is not affected by the interactions of the asperities. To convert Archard's model into the hierarchical framework, the convex hull of each layer,  $j$ , is a sphere of radius,  $R_j$ , where the surface asperity at level  $j$  is given by  $r_j$  and the nominal radius of the smoothed sphere (i.e., without the asperities) is  $r_0$ .



$$R_j = r_j + R_{j+1} = \sum_{i=j}^N r_i$$

EQ 30

The surface patch introduced in section 4 is then used to represent the hierarchical distribution of asperities. Here we use mono-disperse asperity heights at each resolution level and a proportionality constant,  $\alpha$ , such that the asperity height at consecutive scales is related as:

$$R_j = \alpha \cdot r_{j-1}$$

EQ 31

Using an arbitrary  $\alpha$  of 1% for a single sub-resolution level of a rough grain, which has a nominal radius of 100  $\mu\text{m}$ , as shown in Figure 14, is sufficient to reproduce the relationship adapted from Archard [51] for contact of a rough elastic sphere:

$$P \propto A^{5/4},$$

EQ 32

where  $P$  is the load and  $A$  the contact area. The Hertzian solution for a smooth sphere with a radius equal to that of the convex hull for the rough sphere is also shown for comparison (the Hertzian contact observes the relationship  $P \propto A^{3/2}$ ).

Comparison of Archard to Hertzian

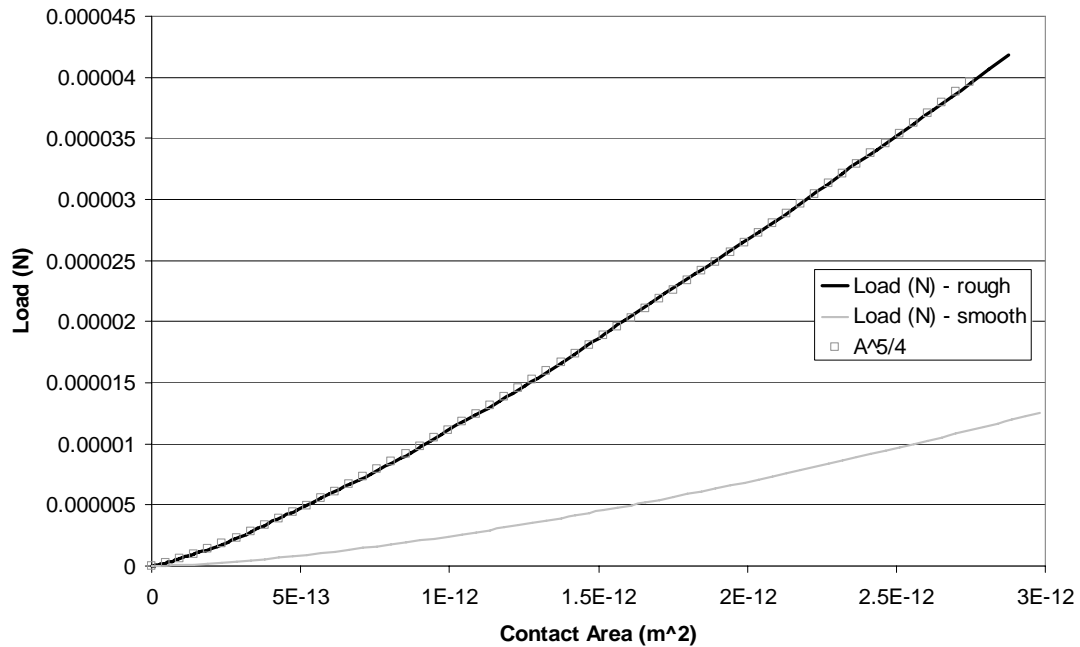


**Figure 14: Comparison of the Archard [51] model as captured by the proposed hierarchical scheme (rough), the Hertzian solution for a smooth sphere (smooth), and the power law relationship derived by Archard for a rough elastic sphere, where the nominal radius is  $100\mu\text{m}$  with  $1\mu\text{m}$  asperities**

## 7. Extensions to Other Surface Phenomena:

A persistent problem in contact mechanics is in determining an effective constitutive law for contact that can handle the full complement of coupled degree-of-freedom reactions of the contact in a computationally efficient manner. Though, detailed finite element modeling of the contact can always be performed (e.g., NIKE2D FEM simulations of Walton et. al. [69]) to finely resolve the contact, this is intractably computationally intensive for multi-body dynamics simulations, as is the molecular dynamics approach of Gilibert [70]. Kalker [71] devoted a significant part of his career to modeling coupled rolling and translational contact. Recent work by Tomas [21, 22] has provided perhaps the most extensive set of contact solutions of appropriate detail for multi-body dynamics simulations. With the detailed capture of traction profiles across the contact areas, the behavior resulting from coupled tractions can be explicitly captured. Though the SDM approach is computationally intensive for massively parallel simulations, it is useful for smaller simulations and as tool in calibrating simpler models of adhesion and contact of rough bodies prior to larger simulations.

For the pharmaceutical manufacturing industry, understanding and controlling the surface adhesion properties of particles is extremely important. From the design of dispersive powder inhalers (DPI's) [72] to the selection and development of powder blenders and the selection of blending excipients, surface adhesion plays a key role in the industrial production of micron-scale powders. For low-shear, blended adhesive pharmaceutical powders, the crushing and surface deformation of individual powder grains is low and the surface morphology relatively constant; therefore, surface properties remain relatively invariant during the process of blending. This invariance can be exploited in the SDM approach to tie microscopic surface properties of the powder grains, such as asperity heights and hydrophilicity, to adhesive strength and functional form of the contact relation.

Several researchers have noted the correlation between relative humidity and powder adhesion. Cleaver and Tyrell [73] offer a survey of the various studies, noting that one of the dominant force mechanisms is the formation of liquid bridges at relative humidity similar to that found in the typical operating environment of pharmaceutical powder blenders. In relatively dry environments, an electrostatic potential may develop at the surface of micron-sized particles, a problem in pharmaceutical processing, lithographic powders [74, 75], the study of solar nebula and cosmic dusts [76, 77], saltation [78], and lunar regolith [79, 80]. In both the cases of electrostatic potential [81] and overall surface energy [82, 83], the surface roughness of the particle has a significant correlation with the magnitude of force developed in the interaction. Coupled with models of liquid bridging [84, 85] and electrostatic potential [78, 86, 87], the SDM method can be used to provide better spatial distribution and coupling of contact effects on the surface of grains.

## **8. Conclusions:**

We have shown a method for capturing phenomena that vary over the surface of powder grains by using a hierarchical, multi-scale discretization of the surface referred to as the SDM method. This computation method allows DEM modelers to easily incorporate theoretical models of surface roughness to multi-body problems. The method has been verified against a sphere coated in a perfectly elastic film where the solution converges to the Hertzian solution for small deformation. The method has also been applied to representing the area of contact for non-adhesive, rough bodies in normal contact and compared against the functional form derived by Archard [51] for contact of rough elastic spheres. The extension to motions along multiple degrees-of-freedom is natural. This approach offers both a method of directly capturing the spatial variance of surface properties in contact laws at arbitrary resolution as well as a method of calibrating existing contact laws for particular materials of interest to the modeler.

This method has applicability beyond the representation of roughness and can be used to design constitutive models of contact based on knowledge of material properties and surface morphology, which can then be used in place of the discretization approach for computational efficiency when implementing in multi-body dynamics simulations. This technique, and the surface discretization framework upon which it is based, can be naturally extended to capture a wide range of other surface-related phenomena. Some examples include: roughness effects (with fine control of asperity scales) in aspherical soil compression; the triboelectric creation and interaction of localized electrostatic charge spots; and the bridging, ion transport, and surface charge-coupled effects of adsorbed water and other volatile compounds.

## **Acknowledgements and Auspices:**

This work was performed under the auspices of the U.S. Department of Energy by Lawrence Livermore National Laboratory under Contract DE-AC52-07NA27344.

The first author wishes to acknowledge the extensive and informative conversations with colleagues at Lawrence Livermore National Laboratory. Dr. Otis Walton provided a wealth of advice on the micromechanics of adhesion. The comments of two anonymous reviewers are also appreciated and contributed greatly to the improvement of this work.

**References:**

1. Hertz H. Über die Berührung fester elastische Körper *Journal für die reine und angewandte Mathematik* 1882; **92**: 156-171
2. Mindlin RD. Compliance of elastic bodies in contact. *Journal of Applied Mechanics* 1949; **71**: 259-268
3. Mindlin RD, Deresiewicz H. Elastic spheres in contact under varying oblique forces. *Journal of Applied Mechanics* 1953; **20**: 269-286
4. Johnson KL, Kendall K, Roberts AD. Surface energy and the contact of elastic solids. *Proceedings of the Royal Society of London* 1971; **324**: 301-313
5. Derjaguin BV, Muller VM, Toporov YP. Effect of contact deformations on the adhesion of particles. *Journal of colloid and interface science* 1975; **53**: 314-326
6. Walton OR, *Force models for particle dynamics simulations of granular materials*, in *Mobile Particulate Systems: Proceedings of the NATO Advanced Study Institute*, E. Guazzelli and L. Oger, Editors. 1994, Kluwer Academic Publishers. p. 367-379.
7. Thornton C, Yin KK, Adams MJ. Numerical simulation of the impact of fracture and fragmentation of agglomerates. *Journal of Physics D: Applied Physics* 1996; **29**: 424-435
8. Owen DRJ, Feng YT, Cottrell MG, Ju J, *Discrete/Finite element modeling of industrial applications with multi-fracturing and particulate phenomena*, in *Discrete Element Methods: Numerical Modeling of Discontinua*, B. K. Cook and R. P. Jensen, Editors. 2002, ASCE: Reston, VA. p. 11-16.
9. Owen DRJ, Feng YT. Parallelised finite/discrete element simulation of multi-fracturing solids and discrete systems. *Engineering Computations* 2001; **18**: 557-76
10. Herbst JA, Potapov AV. Making a Discrete Grain Breakage model practical for comminution equipment performance simulation. *Powder Technology* 2004; **143-144**: 144-150
11. Hertz H. *Journal of Mathematics* 1881; **92**:
12. Walton OR, *Numerical simulation of inelastic frictional particle-particle interactions*, in *Particulate Two-Phase Flow*, M. C. Roco, Editor. 1993, Butterworth-Heinemann: Boston. p. 887-911.
13. Vu-Quoc L, Zhang X. An accurate and efficient tangential force displacement model for elastic frictional contact in particle flow simulations. *Mechanics of Materials* 1999; **31**: 235-269
14. Zhang X, Vu-Quoc L. An accurate elasto-plastic frictional tangential force-displacement model for granular flow simulations: displacement-driven formulation. *Journal of Computational Physics* 2007; **225**: 730-752
15. Thornton C, Yin KK. Impact of elastic spheres with and without adhesion. *Powder Technology* 1991; **65**: 153-166
16. Mullier M, Tüzün U, Walton OR. A single-particle friction cell for measuring contact frictional properties of granular materials. *Powder Technology* 1991; **65**: 61-74
17. Maugis D, Pollock HM. Surface forces, deformations, and adherence at metal microcontacts. *Acta Metallurgica* 1984; **32**: 1323-1334

18. Maugis D. Adhesion of spheres: the JKR-DMT transition using a Dugdale model. *Journal of Colloid and Interface Science* 1992; **150**: 243-269
19. Savkoor AR, Briggs GAD. The effect of tangential force on the contact of elastic solids in adhesion. *Proceedings of the Royal Society A* 1977; **356**: 103-114
20. Luding S, *About contact force-laws for cohesive frictional materials in 2D and 3D*, in *Behavior of Granular Media*, P. Walzel, S. Linz, C. Krülle and R. Grochowski, Editors. 2006, Shaker Verlag: Aachen. p. 137-147.
21. Tomas J. *Micromechanics of particle adhesion*. in *AICHE 2006 Spring National Meeting*. 2006. Orlando, Florida, United States.
22. Tomas J. Adhesion of ultrafine particles-a micromechanical approach. *Chemical Engineering Science* 2007; **62**: 1997-2010
23. Ting JM, Meachum LR, Rowell JD. Effect of particle strength on the strength and deformation mechanisms of ellipse-shaped granular assemblages. *Engineering Computations* 1995; **12**: 99-108
24. Favier JF, Abbaspour-Fard MH, Kremmer H. Modeling nonspherical particles using multisphere discrete elements. *Journal of Engineering Mechanics* 2001; **127**: 971-7
25. Zhou YC, et al. Rolling friction in the dynamic simulation of sandpile formation. *Physica A* 1999; **269**: 536-53
26. Zhou YC, Xu BH, Yu A-B, Zulli P. An experimental and numerical study of the angle of repose of coarse spheres. *Powder Technology* 2002; **125**: 45-54
27. Ting JM, Khwaja M, Meachum LR, Rowell JD. An ellipse-based discrete element model for granular materials. *International Journal for Numerical and Analytical Methods in Geomechanics* 1993; **17**: 603-623
28. Shodja HM, Nezami EG. A micromechanical study of rolling and sliding contacts in assemblies of oval granules. *International Journal for Numerical and Analytical Methods in Geomechanics* 2003; **27**: 403-424
29. Lin X, Ng T-T. Contact detection algorithms for three-dimensional ellipsoids in discrete element modeling. *International Journal for Numerical and Analytical Methods in Geomechanics* 1995; **19**: 653-659
30. Ng T-T. Fabric Study of Granular Materials after Compaction. *Journal of Engineering Mechanics* 1999; **125**: 1390-1394
31. Ouadfel H, Rothenburg L. An algorithm for detecting inter-ellipsoid contacts. *Computers and Geotechnics* 1999; **24**: 245-263
32. Mustoe GGW, Miyata M. Material Flow Analyses of Noncircular-Shaped Granular Media Using Discrete Element Methods. *Journal of Engineering Mechanics* 2001; **127**: 1017-1026
33. Kuhn MR. Smooth convex three-dimensional particle for the discrete-element method. *Journal of Engineering Mechanics* 2003; **129**: 539-547
34. Johnson SM, Williams JR, Cook BK. Contact resolution algorithm for an ellipsoid approximation for discrete element modeling. *Engineering Computations* 2004; **21**: 215-34
35. Greenwood JA, Williamson JBP. Contact of nominally flat surfaces. *Proceedings of the Royal Society A* 1966; **295**: 300-319
36. Greenwood JA, Tripp JH. The elastic contact of rough spheres. *Journal of Applied Mechanics* 1967; **34**: 153-159

37. Ciavarella M, Delfine V, Demelio G. A "re-vitalized" Greenwood and Williamson model of elastic contact between fractal surfaces. *Journal of the Mechanics and Physics of Solids* 2006; **54**: 2569-2591
38. Majumdar A, Bhushan B. Fractal model of elastic-plastic contact between rough surfaces. *Journal of Tribology* 1991; **113**: 1-11
39. Chang RW, Etison I, Bogy DB. Static friction coefficient model for metallic rough surfaces. *ASME Journal of Tribology* 1988; **110**: 57-63
40. Hurtado JA, Kim K-S. Scale effects in friction of single asperity contacts: part 1; from concurrent slip to single-dislocation-assisted slip *Proceedings of the Royal Society A* 1999; **455**: 3363-3384
41. Hurtado JA, Kim K-S. Scale effects in friction of single asperity contacts: part 2; multiple-dislocation-cooperated slip. *Proceedings of the Royal Society A* 1999; **455**: 3385-3400
42. Adams GG, Müftü S, Mohd Azhar N. A nano-scale multi-asperity model for contact and friction. in *2002 ASME/STLE Tribology Conference*. 2002. Cancun, Mexico.
43. Adams GG, Müftü S, Mohd Azhar N. A nano-scale multi-asperity contact and friction model. *ASME Journal of Tribology* 2003; **125**: 700-708
44. Johnson SM, *Resolution of grain scale interactions using the discrete element method*, in *Department of Civil and Environmental Engineering*. 2006, Massachusetts Institute of Technology: Cambridge, MA. 224.
45. Johnson SM, Williams JR, Cook BK. A modeling approach for cohesive powder processing. in *Discrete Element Methods 2007*. 2007. Brisbane, Australia.
46. Mendez-Villas A, Nuevo MJ, Gonzalez-Martin ML. On the use of RMS roughness for surface roughness characterization. *Material Science Forum* 2002; **408**: 245-250
47. Sayles RS, Thomas TR. Surface topography as a non-stationary random process. *Nature* 1978; **271**: 424-431
48. Majumdar A, Bhushan B. Role of fractal geometry in roughness characterization and contact mechanics of surfaces. *ASME Journal of Tribology* 1990; **112**: 205-216
49. Odagi K, Tanaka T, Yamane K. *Rough-surface model and its applications to DEM simulation of compression test of particles*. in *Discrete Element Methods: Numerical Modeling of Discontinua*. 2002. Santa Fe, NM: ASCE.
50. Archard JF. Elastic deformation and the laws of friction. *Proceedings of the Royal Society A* 1957; **243**: 190-205
51. Archard JF. Contact and rubbing of flat surfaces. *Journal of Applied Physics* 1953; **24**: 981-988
52. Fuller KNG, Tabor D. The effect of surface roughness on the adhesion of elastic solids. *Proceedings of the Royal Society A* 1975; **345**: 327-342
53. Thomas TR, Sayles RS. Random-process approach to the prediction of joint stiffness. *Transactions of ASME: Journal of Engineering for Industry* 1977; **99B**: 250-256
54. Sramek M. *High precision non-binary voxelization of geometric objects*. in *17th Spring Conference on Computer Graphics (SCCG01)*. 2001. Slovakia.

55. Garboczi EJ. Three-dimensional mathematical analysis of particle shape using X-ray tomography and spherical harmonics: application to aggregates used in concrete. *Cement and Concrete Research* 2002; **32**: 1621?-1638
56. Li Q, et al. Implicit fitting using radial basis functions with ellipsoidal constraint. *Computer Graphics* 2004; **23**: 55-69
57. Schroeder P, Sweldens W. Spherical wavelets: efficiently representing functions on the sphere. *Computer Graphics* 1995; **29**: 161--172
58. Williams JR, Amaratunga K. *Wavelet representation of geometry for analysis*. in *Proceedings of the Second International Conference on Discrete Element Methods (DEM)*. 1993. Cambridge, MA, USA: AFOSR.
59. Amaratunga K. A wavelet-based approach for compressing kernel data in large-scale simulations of 3D integral problems. *IEEE Computing in Science and Engineering* 2000; **2**: 34-45
60. Amaratunga K, Castrillon-Candas JE. Surface Wavelets: A Multiresolution Signal Processing Tool for 3D Computational Modeling. *International Journal for Numerical Methods in Engineering* 2001; **52**: 239-271
61. Munjiza A, Bicanic N, Owen DRJ. *BSD contact detection algorithm for discrete elements in 2D*. in *Proceedings of the Second International Conference on Discrete Element Methods (DEM)*. 1993. Cambridge, MA, USA: AFOSR.
62. Wensel O, Bicanic N. *A quad tree based contact detection algorithm*. in *Proceedings of the Second International Conference on Discrete Element Methods (DEM)*. 1993. Cambridge, MA, USA: AFOSR.
63. Ristow GH. Granular Dynamics: A Review about recent Molecular Dynamics Simulations of Granular Materials. *Annual Reviews of Computational Physics* 1994:
64. Williams JR, O'Connor RM. A linear complexity intersection algorithm for discrete element simulation of arbitrary geometries. *International Journal for Numerical and Analytical Methods in Geomechanics* 1995; **12**: 185-201
65. Munjiza A, Andrews KRF. NBS contact detection algorithm for bodies of similar size. *International Journal for Numerical Methods in Engineering* 1998; **43**: 131-149
66. Perkins ED, Williams JR. A fast contact detection algorithm insensitive to object sizes. *Engineering Computations* 2001; **18**: 48-61
67. Perkins ED, Williams JR, *Generalized spatial binning of bodies of different sizes*, in *Discrete Element Methods: Numerical Modeling of Discontinua*, B. K. Cook and R. P. Jensen, Editors. 2002, ASCE: Reston, VA, USA.
68. Williams JR, Perkins ED, Cook BK. A contact algorithm for partitioning N arbitrary sized objects. *Engineering Computations* 2003; **21**: 235-248
69. Walton OR, Brandeis J, Cooper JM. *Modeling of inelastic, frictional, contact forces in flowing granular assemblies*. in *21st Annual Meeting of the Society of Engineering Science*. 1984. Blacksburg, VA, USA.
70. Gilabert FA, Krivtsov AM, Castellanos A. A molecular dynamics model for single adhesive contact. *Meccanica* 2006; **41**: 341-349
71. Kalker JJJ, *Three-dimensional elastic bodies in rolling contact*. Springer-Verlag: New York, NY, USA, 1990

72. Chew NYK, Chan H-K. The Role of Particle Properties in Pharmaceutical Powder Inhalation Formulations. *Journal of Aerosol Medicine* 2002; **15**: 325-330
73. Cleaver JAS, Tyrrell JWG. The influence of relative humidity on particle adhesion – a review of previous work and the anomalous behaviour of soda-lime glass. *KONA* 2004; **22**:
74. Feng JQ. Electrostatic interaction between two charged dielectric spheres. *Physical Review E* 2000; **62**: 2891-2897
75. Feng JQ, Hays DA. Relative importance of electrostatic forces on powder particles. *Powder Technology* 2003; **135-136**: 65-75
76. Desch SJ, Cuzzi JN. The generation of lightning in the solar nebula. *Icarus* 2000; **143**: 87-105
77. Poppe T, Schraeppler R. Further experiments on collisional tribocharging of cosmic grains. *Astronomy & Astrophysics* 2005; **438**: 1-9
78. Kok JE, Renno NO. Electrostatics in wind-blown sand. *Physical Review Letters* 2008; **100**: 014501-1-4
79. Sternovsky Z, et al. Contact charging of lunar and Martian dust simulants. *Journal of Geophysical Research* 2002; **107**: 15-1-8
80. Walton OR, *Adhesion of Lunar Dust*, NASA, 'Editor'. 2007, NASA: Hanover, MD. 48.
81. Sun N, Walz JY. A Model for Calculating Electrostatic Interactions between Colloidal Particles of Arbitrary Surface Topology. *Journal of Colloid and Interface Science* 2001; **234**: 90-105
82. Domike R, *Pharmaceutical Powders in Experiment and Simulation : Towards a Fundamental Understanding*, in *Department of Chemical Engineering*. 2004, Massachusetts Institute of Technology: Cambridge, Massachusetts
83. Ngai S, *Multi-Scale Analysis and Simulation of Powder Blending in Pharmaceutical Manufacturing*, in *Department of Chemical Engineering*. 2005, Massachusetts Institute of Technology: Cambridge, MA. 228.
84. Lian G, Thornton C, Adams MJ. A theoretical study of the liquid bridge forces between two rigid spherical bodies. *Journal of colloid and interface science* 1993; **161**: 138-147
85. Thornton C, Lian G, Adams MJ. *Modeling liquid bridges between particles in DEM simulations of particle systems*. in *Proceedings of the Second International Conference on Discrete Element Methods (DEM)*. 1993. Cambridge, MA, USA: AFOSR.
86. Lacks DJ, Levandovsk A. Effect of particle size distribution on the polarity of triboelectric charging in granular insulator systems. *Journal of Electrostatics* 2007; **65**: 107-112
87. Duff N, Lacks DJ. Particle dynamics simulations of triboelectric charging in granular insulator systems. *Journal of Electrostatics* 2008; **66**: 51-57